Nanoscaffold effects on the performance of air-cathodes for microbial fuel cells: Sustainable Fe/N-carbon electrocatalysts for the oxygen reduction reaction under neutral pH conditions

Alessandro Iannaci [a], Swapnil Ingle [a], Carlota Domínguez [a], Mariangela Longhi [b],
Odile Merdrignac-Conanec [c], Soraya Ababou-Girard [d], Frédéric Barrière [c,*], Paula E. Colavita [a,*]

[a] School of Chemistry, CRANN and AMBER Research Centres, Trinity College Dublin, College Green, Dublin 2, Ireland
[b] Università degli Studi di Milano, Dipartimento di Chimica, Via Golgi 19, 20133 Milano, Italy
[c] Univ Rennes, CNRS, Institut des Sciences Chimiques de Rennes – UMR 6226, F-35000 Rennes, France
[d] Univ Rennes, CNRS, Institut de Physique de Rennes, UMR 6251, F-35000 Rennes, France

ARTICLE INFO

ABSTRACT

Nanostructured electrocatalysts for microbial fuel cell air-cathodes were obtained via use of conductive carbon blacks for the synthesis of high performing 3D conductive networks. We used two commercially available nanocarbons, Black Pearls 2000 and multiwalled carbon nanotubes, as conductive scaffolds for the synthesis of nanocomposite electrodes by combining: a hydrothermally carbonized resin, a sacrificial polymeric template, a nitrogenated organic precursor and iron centers. The resulting materials are micro-mesoporous, possess high specific surface area and display N-sites (N/C of 3–5 at%) and Fe-centers (Fe/C < 1.5 at.%) at the carbon surface as evidenced from characterization methods. Voltammetry studies of oxygen reduction reaction activity were carried out at neutral pH, which is relevant to microbial fuel cell applications, and activity trends are discussed in light of catalyst morphology and composition. Tests of the electrocatalyst using microbial fuel cell devices indicate that optimization of the nanocarbon scaffold for the Pt-free carbon-based electrocatalysts results in maximum power densities that are 25% better than those of Pt/C cathodes, at a fraction of the materials costs. Therefore, the proposed Fe/N-carbon catalysts are promising and sustainable high-performance cathodic materials for microbial fuel cells.

1. Introduction

Air and water pollution caused by combustion of fossil fuels for human activities is one of the most important problems of this century and research on alternative environmentally friendly energy sources is a paramount scientific, economic and social objective [1]. By 2100, the energy consumption rate is projected to increase up to three times the present value [2]; while photovoltaic, wind and geothermal renewable sources are expected to gradually replace power from fossil fuels, their availability is skewed and highly dependent on geographical distribution [3]. Therefore, it would be desirable to also develop technologies based on renewables with more uniformly distributed or complementary availability, such as those based on waste valorization or bio-waste exploitation.

Microbial fuel cells (MFCs) can be considered as an interesting family of green technologies that allows for power generation from anaerobic digestion of organic waste or biomass by *exoelectrogen* biofilms developed at the anodic MFC compartment [4–7]. Waste-fuel is processed via electrocatalysis at the bioanode and much attention has been devoted to the optimization of bioanode nanostructure, bio-interface and bacterial consortia, including by our group [8–16]; however, the overall MFC device performance is strongly dependent also on activity at the cathode. In the cathodic compartment, a range of electron acceptors can be used [4]; notably, oxygen is one of the most desirable acceptor species for MFC applications because it can be readily available at low cost and large scale via simple aeration of the catholyte. Use of oxygen can however result in significant power losses due to the sluggishness of the oxygen reduction reaction (ORR): this is a multi-step, multi-electron reduction process that requires the use of precious metal electrocatalysts such as Pt/C to avoid kinetic losses in fuel cell devices [17–20]. The use of precious metal catalysts for the ORR at MFC cathodes represents a significant drawback as Pt load-

---

* Corresponding authors.
  E-mail addresses: frederic.barriere@univ-rennes1.fr (F. Barrière), colavitp@tcd.ie (P.E. Colavita).

ings can account for up to 47% of the overall MFC costs [5,21]. Importantly, typical operational conditions for ORR cathodes in MFCs, namely ambient temperature, near-neutral pH, and low purity catholytes, are not ideal for Pt-based catalysis [22–24], further limiting MFC performance when employing these otherwise high-performing electrocatalysts [25,26].

The reduction of Pt loadings or the complete replacement of precious metals with more sustainable catalysts would be therefore highly desirable and could enable the implementation of MFC technologies at greater scale and at lower costs. Recent breakthroughs in the synthesis of non-Pt group catalysts for the ORR in hydrogen fuel cells suggest this is a realistic goal, and several examples of advanced electrode materials with high activity in the ORR in the absence of precious metals have been reported [27,28]. High activity in the ORR can be achieved using low cost materials by combining transition metals (e.g. Fe, Co, Mn) with carbon materials and nanomaterials. Among the cited transition metals iron is particularly interesting for scalable applications in sustainable technologies due to its low cost and high-abundance. The carbon support/scaffold plays a crucial role in the design of MFC cathodes: in general, it is chosen to display both high specific surface area and high conductivity, to increase the density of active sites and minimize ohmic losses, respectively [29–31]. Heteroatom functionalization, in particular nitrogenation, of the carbon scaffold is an important strategy for the design of ORR-active materials [27,28]: functional groups can result in improved wetting, stability, porosity, conductivity [32–34] and, importantly, regulate ORR intrinsic activity and selectivity towards the 4-electron reduction product [35–37].

Several groups have recently demonstrated that the combination of transition metals and nitrogen-doped carbon materials offers a successful strategy for the replacement of Pt-group catalysts in MFC air-cathodes [5,38–48]. A variety of iron-containing organic precursors has been explored for the synthesis of Fe/C electrocatalysts for MFCs, such as ethylenediaminetetraacetic acid, iron acetate, iron phthalocyanine, and Cl-Fe^{III} tetramethoxyphenylporphyrin [5,38,42,43,46,49–51]. Nitrogenation of the carbon structure alone has also been explored with a variety of methods [52–54]. Carbon nanomaterials such as nanotubes and graphene have been used as conductive supports in the synthesis of air-cathodes for MFCs, given that they display excellent conductivity and can be used to fabricate electrodes with high specific surface area, complex chemistry and advanced 3D architectures. However, these nanocarbons are more expensive and difficult to process [4] relative to low cost carbon conductive fillers currently produced in large scale. Commercial conductive carbon blacks are nanocarbons (primary particle size 10–30 nm) that can display excellent properties as electrode and catalyst support materials; they can be synthesized with high purity and in large scales (megatons/annum) at modest costs [55] and, hence, are ideal for applications in MFC devices. In this work, we report on the development of nanostructured Fe/carbon based electrocatalysts obtained via use of conductive carbon blacks as the nanomaterial scaffold for the synthesis of high performing 3D conductive networks.

Commercially available carbon Black Pearls 2000 were used as a nanocarbon scaffold for the synthesis of nanocomposite electrodes via a combination of a hydrothermally carbonized resin, a sacrificial polymeric template and iron centers. The materials were characterized to determine surface composition, pore structure and specific surface area; their electrocatalytic activity in the ORR was studied at neutral pH using voltammetry and their performance as air-cathodes was assessed in dual-chamber MFC devices. The properties and activity of the electrode materials were compared to those of analogue electrodes prepared using multiwall carbon nanotubes, instead, as the nanocarbon scaffold, thus enabling a direct comparison of performances between a commer-

cial carbon black and the more expensive highly conductive nanomaterial scaffold. Our results show that the low-cost and environmentally safe carbon blacks offer an excellent platform for the fabrication of high performing MFC air-cathodes with high specific surface area and fast kinetics in neutral media.

2. Experimental methods

2.1. Materials

Iron (II) acetate (95%), Nafion® 117 5% solution, resorcinol (99%), Pluronic F-127, melamine (99%), hydrochloric acid (37%), sulfuric acid (95–98%), nitric acid ($\geq$65%), sodium phosphate monobasic (ReagentPlus $\geq$ 99%), sodium phosphate dibasic (BioReagent $\geq$ 99%), sodium acetate (BioXtra $\geq$ 99%), potassium chloride (BioXtra $\geq$ 99%), formaldehyde solution (37 wt%, ACS reagent), hydrogen peroxide (30%), ammonium chloride (min. 99.5%), and multiwalled carbon nanotube (MWCNT) (50–90 nm diameter, >95% carbon basis) were all purchased from Sigma Aldrich. Pt/C 10 wt% was purchased from Quintech; potassium hexacyanoferrate(III) (ACS reagent $\geq$ 99%) was purchased from Fluka. Black Pearls® (BP, average particle size 15 nm [56]) were purchased from Cabot, glassy carbon disks (5 mm o.d.) were purchased from HTW GmbH, graphite rods (GR) were purchased from Morgan Carbon. Fumasep FTAM-E anion exchange membrane PET-reinforced was purchased from Fumatech BWT and carbon cloth with deposited microporous layer was purchased from FuelCellStore.

2.2. Materials synthesis

Prior to modifications, BP and MWCNT were subject to oxidative treatment to remove metal impurities and improve hydrophilicity [5,57,58]: materials were refluxed in concentrated HNO$_3$ at 90 °C for 4 h, then filtered and washed with distilled water until neutral pH was obtained. The resulting carbon paste was dried overnight at 70 °C and finally ground in an agate mortar [43]. Porous carbon-based catalysts were prepared as follows: resorcinol (1.65 g), Pluronic F127 (2.5 g) and melamine (0.84 g) were dissolved in 40 mL of 1:1 water:ethanol solution by volume, followed by stirring for 15 min; the procedure for preparation of Fe-based catalysts also included addition of Fe(CH$_3$COO)$_2$ (1.5 g) to this mixture. Subsequently, concentrated HCl (0.2 g) were added to the above mixture, followed by stirring for 1 h. Formaldehyde solution (2.5 g) was added drop wise under stirring to the mixture, which was further stirred vigorously for another 1 h yielding a homogeneous slurry. The previously purified nanocarbon scaffolds (BP or MWCNT, 1.5 g) were then added to the dispersion and stirred for another 15 min. This mixture was transferred to a Teflon-lined autoclave that was heated in an oven at 50 °C for 2 days; the sample was then removed from the autoclave and dried for 2 days at 60 °C. The resulting powder was ground in a mortar and further dried in a tube furnace (110 °C, 25 min) under nitrogen flow (200 sccm) and, subsequently annealed (800 °C, 2 h) under flow using N$_2$:NH$_3$ 1:1 vol (200 sccm) followed by rapid cooling under N$_2$. Materials resulting from synthesis in the presence and absence of iron acetate are referred to as FeRPMX and RPMX, respectively, where X = BP or CNT in the case of BP or MWCNT being used as nanocarbon scaffolds, respectively and RPM = Resorcinol, Pluronic and Melamine.

2.3. Characterization

Brunauer-Emmett-Teller (BET) specific surface areas were obtained from the N$_2$ adsorption isotherms at 77 K measured on

Table 1

Summary of bulk atomic %-composition (equivalent to molar-%) resulting from elemental analysis and ICP-OES determinations of metal content; and results from BET determinations of specific surface area.

Sample Name	Atomic-%					Specific surface area ($m^2 \ g^{-1}$)
	N	C	H	O	Fe	
RPM_CNT	1.48	85.17	8.06	5.29	–	293
RPM_BP	4.20	78.91	6.26	10.63	–	651
FeRPM_CNT	1.30	81.65	6.34	9.35	1.35	231
FeRPM_BP	2.88	74.94	11.02	10.7	0.45	485

a Gemini VII volumetric adsorption analyzer from Micromeritics (Norcross, GA, USA). Before measurement, powdered samples were outgassed at 250 °C overnight in a VacPrep 061 degas system to remove adsorbed and undesired species from the sample surface. Specific surface areas were derived from the isotherms using the BET equation and a set of 9 experimental points of the linear range of the BET plot ($0.05 \leq P/P^0 \leq 0.3$). Pore size distributions were evaluated by Barrett-Joyner-Halenda (BJH) mesopore analysis method. A JEOL JEM 2100 transmission electron microscope (TEM) with LaB_6 gun operated at 200 kV was used for sample morphology evaluation. The fine structures were observed by FEI Titan 80–300 instrument with Schottky field emission electron source operated at 300 kV equipped with Gatan Tridiem spectrometer for the electron energy loss spectroscopy (EELS) used for elemental analysis. Samples for TEM observation were prepared by drop and dry technique as follows: samples in form of dry powder were dispersed in deionized water, sonicated 5 min, then dropped on carbon-coated copper TEM meshes and dried in air. Images were analyzed using free software (ImageJ 1.50b). X-ray photoemission spectroscopy (XPS) was performed in a ultra-high vacuum chamber with base pressure $<10^{-9}$ mbar, equipped with a dual anode source (Al K_α at 1486.6 eV and Mg K_α at 1253.6 eV). Spectra were collected at a 0° take-off angle with 20 eV pass energy; binding energies are calibrated relative to the C 1s line (284.6 eV). Atomic %-ratios were obtained from ratios of peak areas in the high resolution spectra, after correction by Scofield relative sensitivity factors for the relevant photoemission lines ($N1s_{Mg}$ = 1.77, $O1s_{Mg}$ = 2.85 and $Fe2p_{3/2Mg}$ = 10.54; $N1s_{Al}$ = 1.8, $O1s_{Al}$ = 2.93 and $Fe2p_{3/2Al}$ = 10.82). Elemental microanalysis (CHNS) was carried out on a ThermoFinnigan FlashEA1112Series; oxygen wt.% content was calculated as the balance of the total. Metal concentrations were determined via inductively coupled plasma-optical emission spectroscopy (iCAP 7000 ICP-OES Analyser, Thermo Fisher). Electrochemical characterization was carried out using a potentiostat (Metrohm Autolab) and a 3-electrode cell with Saturated Calomel Electrode (IJ Cambria) as reference electrode, a graphite rod as counter electrode, and a (modified) glassy carbon rotating disk electrode (RDE, Metrohm RDE2, 0.07065 cm^2 geometric area) as working electrode. Catalytic inks were prepared as follows: 10 mg of catalyst was dispersed in 135 μL of ultrapure water, 270 μL of ethanol, 50 μL of Nafion 117 (5% solution) followed by sonication (20 min). The obtained ink was drop cast (3.55 μL) over the RDE surface and dried under air, resulting in a catalyst load of 1.10 mg cm^{-2}. Prior to all experiments, the electrochemical cell was cleaned using piranha solution, washed with ultrapure water and filled with 0.05 M Na_2HPO_4/NaH_2PO_4 solution (pH 7.2). Prior to experiments the electrolyte was purged with Ar for 20 min; 10 cyclic voltammograms (CV) were first recorded at 50 mV s^{-1} over the potential window of interest, followed by two CVs at 5 mV s^{-1}. The solution was then purged with O_2 (medical grade) for 20 min and CVs were recorded at 2500, 1600, 900, 400 and 0 rpm at 5 mV s^{-1}; two cycles were collected at each rotation rate, with the second scan being the one shown in all figures. All data is shown after subtraction of capacitive contributions determined as the background CV in Ar-purged electrolyte; measurements were

iR-compensated based on determinations of impedance at open circuit voltage, using commercial software (NOVA) [59]. Mass activity calculations were performed following published protocols [60]. Faradaic current densities (J_F in mA cm^{-2}) were obtained by subtracting the capacitive current obtained in Ar-saturated electrolyte from that obtained in O_2-saturated electrolyte, at 1600 rpm rotation rate, under identical experimental conditions. ORR kinetic current densities J_k (mA cm^{-2}) were calculated as: $J_k = \frac{J_F * J_{LIM}}{(J_{LIM} - J_F)}$, where J_{LIM} is the limiting current. Finally, the ORR mass activity was obtained from $I_M = \frac{J_k}{M_{cat}}$ where M_{cat} is the total catalyst loading (1.10 mg cm^{-2}). Area activities were calculated from the Faradic currents, I_F, of each electrode at 1600 rpm; the total surface area of the loaded catalyst A (m^2) was calculated from the catalyst amount deposited over the disk (7.7×10^{-5} g), multiplied by the BET specific surface area. Finally, specific area activities were calculated as: $\frac{I_F}{A}$. Unless otherwise specified, error bars are calculated on the basis of data from three replicates.
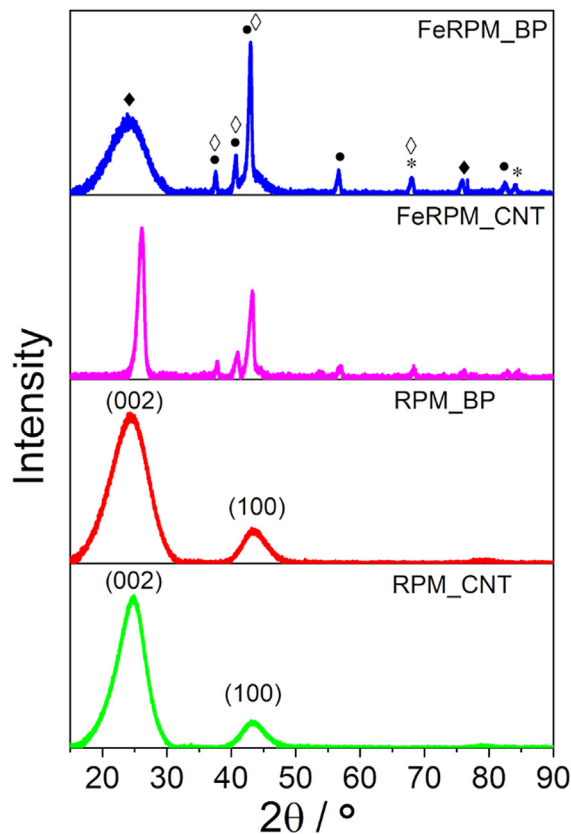
Fig. 1. XRD patterns of FeRPM_BP, FeRPM_CNT and the corresponding Fe-free carbon materials RPM_BP and RPM_CNT; (♦) graphitic carbon, (●) Fe_2N, (◇) Fe_3N, (*) Fe_3C.

2.4. Microbial Fuel Cells (MFC) characterizations

Double chamber MFC devices were fabricated as previously reported [8] with *ca.* 85 mL capacity in each compartment and a circular membrane 1.8 cm in diameter. Graphite rod (GR) electrodes used in MFC devices were polished with sand paper (1200 grit) and subsequently sonicated in water, acetone and methanol (5 min in each solvent) prior to use; GRs were suspended in each compartment using rubber septa. The anodic solution consisted of 50/50 vol% wastewater (Beaurade Wastewater Treatment Plant, Rennes, France) and phosphate buffer saline (PBS) solution consisting of 0.032 M Na_2HPO_4, 0.018 M NaH_2PO_4, 6.0 mM NH_4Cl and 2.0 mM KCl. Sodium acetate was added as a nutrient to the resulting mixture of PBS and wastewater, resulting in a final sodium acetate concentration of 0.012 M [8]. A cathodic solution consisting of 0.1 M $K_3[Fe(CN)_6]$ in 0.032 M Na_2HPO_4 and 0.018 M NaH_2PO_4 was used during the acclimation process of the biofilm community; the hexacyanoferrate (III) served as the electron acceptor and the 0.1 M concentration was confirmed to ensure a stable cathodic potential. MFC air-cathodes were prepared following a previous published procedure [43,61]: briefly, a suspension of 5 mg catalyst in 41.5 μL of H_2O with 33.4 μL of Nafion and 16.7 μL of EtOH was sonicated (20 min) and then drop-cast over 1 cm^2 carbon cloths and dried overnight. Pt/C catalyst (10% w/w Pt, Quintech) was used as control with loading and deposition procedure that was identical to that of carbon electrocatalysts (5 mg cm^{-2}).

The cells were connected to a 1000 Ω resistance during acclimation; voltage outputs were acquired each day with a multimeter to monitor biofilm development. Once a stable MFC voltage was obtained, the cathodic solution was removed and replaced with 0.05 M Na_2HPO_4/NaH_2PO_4 solution (pH 7.2) for air–cathode testing. Carbon cloth cathodes were introduced in each MFC chamber and O_2 was bubbled (20 min) prior to measurements. Power density curves were acquired by varying the external resistance (10,000–10 Ω) at 30 min intervals and measuring the cell voltage at each resistance; the resistances used were: 4 MΩ (OCV), 10,000, 5000, 2500, 1000, 500, 250, 100, 50, 25 and 10 Ω. All measurements were carried out at room temperature (20 ± 1 °C) on three independent replicates for each cathode. Power density (mW m^{-2}) and current density (mA m^{-2}) were calculated normalizing by the geometric area of the carbon cloth (1 cm^2). After each set of power density measures, MFC were left in thermal bath (25 ± 1 °C) with a 0.1 M $K_3[Fe(CN)_6]$ solution refilled in the cathodic compartment and again connected to a 1000 Ω resistance. In order to maintain the bioanodes, sodium acetate (0.012 M) was added when the measured voltage of each cell decreased below 0.05 V.

3. Results and discussion

3.1. Physical characterization of carbon-based electrocatalysts

Carbon materials were synthesized using a protocol that combines highly conductive carbon scaffolds with functional porous shells: the presence of a porous shell allows for high specific surface area and incorporation of the metal-centers, while maintaining high conductivity via formation of 3D networks of interconnected nanocarbon. The synthesis protocol was adapted from work by Karthik et al. [62] on the synthesis of N-free, macro-mesoporous monoliths using resorcinol–formaldehyde
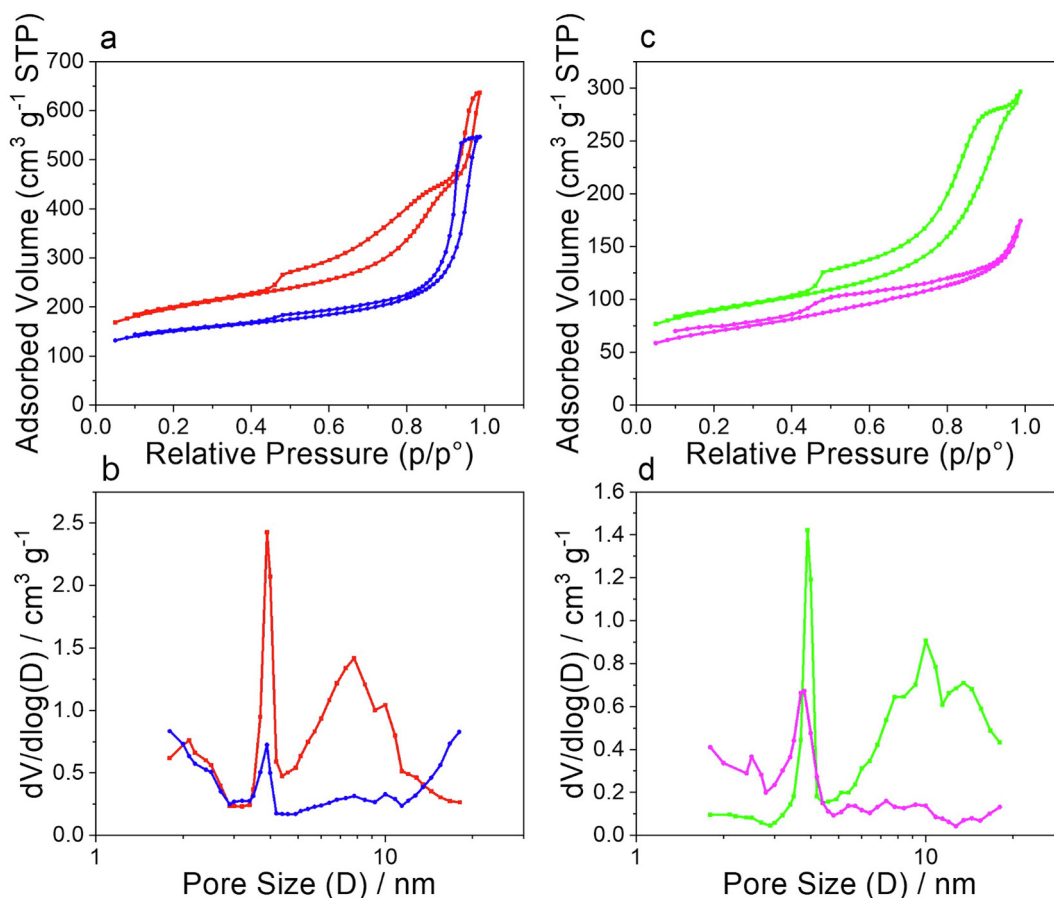
Fig. 2. (a) Nitrogen adsorption isotherms and (b) pore distributions obtained for materials prepared using BP as nanocarbon scaffolds; (━) RPM_BP, (━) FeRPM_BP. (c) Nitrogen adsorption isotherms and (d) pore distributions obtained for materials prepared using MWCNT as nanocarbon scaffolds; (━) RPM_CNT, (━) FeRPM_CNT.

resins on insulating foam supports. In this work, resorcinol–formaldehyde resins were prepared with inclusion of melamine and iron acetate, as sources of nitrogen and iron, respectively. Reactants for the synthesis of the resins were blended with either carbon blacks (FeRPM_BP) or MWCNT (FeRPM_CNT) to impart high conductivity, and with a sacrificial polymeric template. These mixtures were hydrothermally treated, subsequently annealed, and the resulting materials were then characterized and investigated for electrode applications. The Fe-free carbon materials RPM_BP and RPM_CNT were synthesized by omitting the iron acetate in the resin/nanocarbon blends; these were also studied to better understand the effects of Fe-centers on structure and activity.

The bulk composition of the materials was investigated via elemental analysis (CHNS) and ICP-OES to determine the relative ratios of light atoms and the Fe wt.% content, respectively; Table 1 summarizes the atomic composition of the four materials prepared, calculated by combining the results from both methods (see Supporting Information, **Table S1**). Results indicate all four materials consist mostly of carbon with small amounts of hydrogenated groups, as expected of materials that undergo graphitization under inert atmosphere. The nitrogen content varies in the range 1.0–4.5 at.%, while the Fe at.% content was found to be 1.35% and 0.45% for FeRPM_CNT and FeRPM_BP, respectively. XRD was further used to investigate bulk composition; Fig. 1 shows XRD patterns for FeRPM_BP and FeRPM_CNT, and for the metal-free RPM_BP and RPM_CNT. Fe-free samples show two broad peaks at *ca.* 25° and another at *ca.* 43° that are assigned to the (0 0 2) and (1 0 0) diffractions of carbon, respectively [62], where their peak width indicates poor crystallinity. This suggests that in the absence of Fe centers, diffraction patterns are dominated by contributions from carbonized material with poor crystallinity. Broad contribu-

tions at the same 2θ values are observed in the case of FeRPM_BP, whereas only sharp peaks are evident in the FeRPM_CNT sample. This indicates that under the same annealing conditions, the average size of graphitic crystallites achieved for FeRPM_CNT is much larger [31,62,63]. Additional peaks in the patterns of FeRPM_BP and FeRPM_CNT are observed at 38°, 41°, 54°, 57°, 68° and 76°; these are assigned to contributions from nitrides and carbides, in agreement with reference patterns for Fe_2N (PDF#73–2102), Fe_3N (PDF#01–1236) and Fe_3C (PDF#89–2005). Formation of nitrides and carbides is consistent with a process involving carbonization of the organic resin under the N-rich ammonia atmosphere while in the presence of iron salts, and is consistent with previously observed results of pyrolysis reactions under similar conditions [63,64].

Specific surface area and pore structure were determined by BET analysis and Barrett-Joyner-Halenda (BJH) analysis methods of N_2 sorption isotherms, respectively; a summary of BET areas is reported in Table 1. Materials prepared with BP scaffolds yielded higher BET areas (651 and 485 $m^2 g^{-1}$) than their CNT-based counterparts (293 and 231 $m^2 g^{-1}$), which is consistent with BP possessing an area [65,66] >1400 $m^2 g^{-1}$ compared to <300 $m^2 g^{-1}$ for MWCNT [67]. Incorporation of iron in the resin results in specific surface areas that are 22–25% lower than that of the Fe-free equivalent material; this is in agreement with previous literature reports that show that, during the pyrolysis of organic precursors, iron catalyzes gasification and graphitization, leading to pore opening and lower BET areas than in the absence of iron in the carbon structure [68,69]. Fig. 2 shows isotherms and pore size distributions (PSDs) of the nitrogen-doped carbon based catalysts: all of the considered materials exhibit hysteresis loops characteristic of the type IV isotherm associated with capillary condensation, typically observed
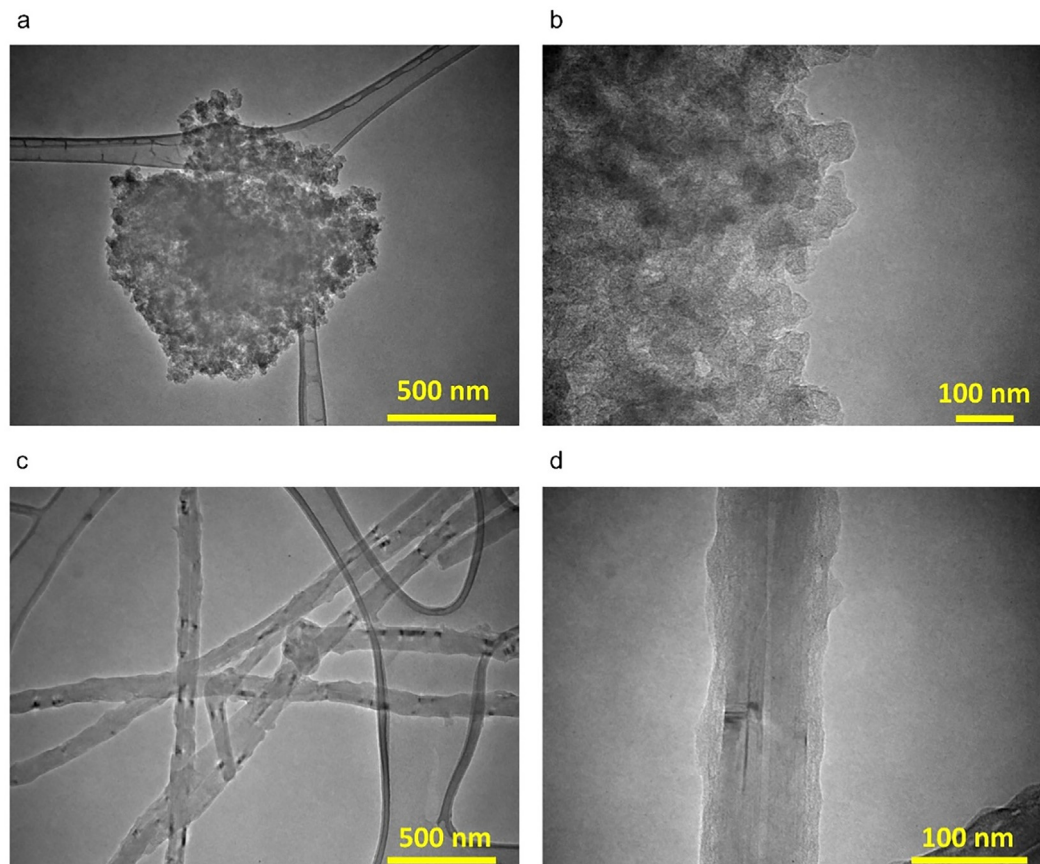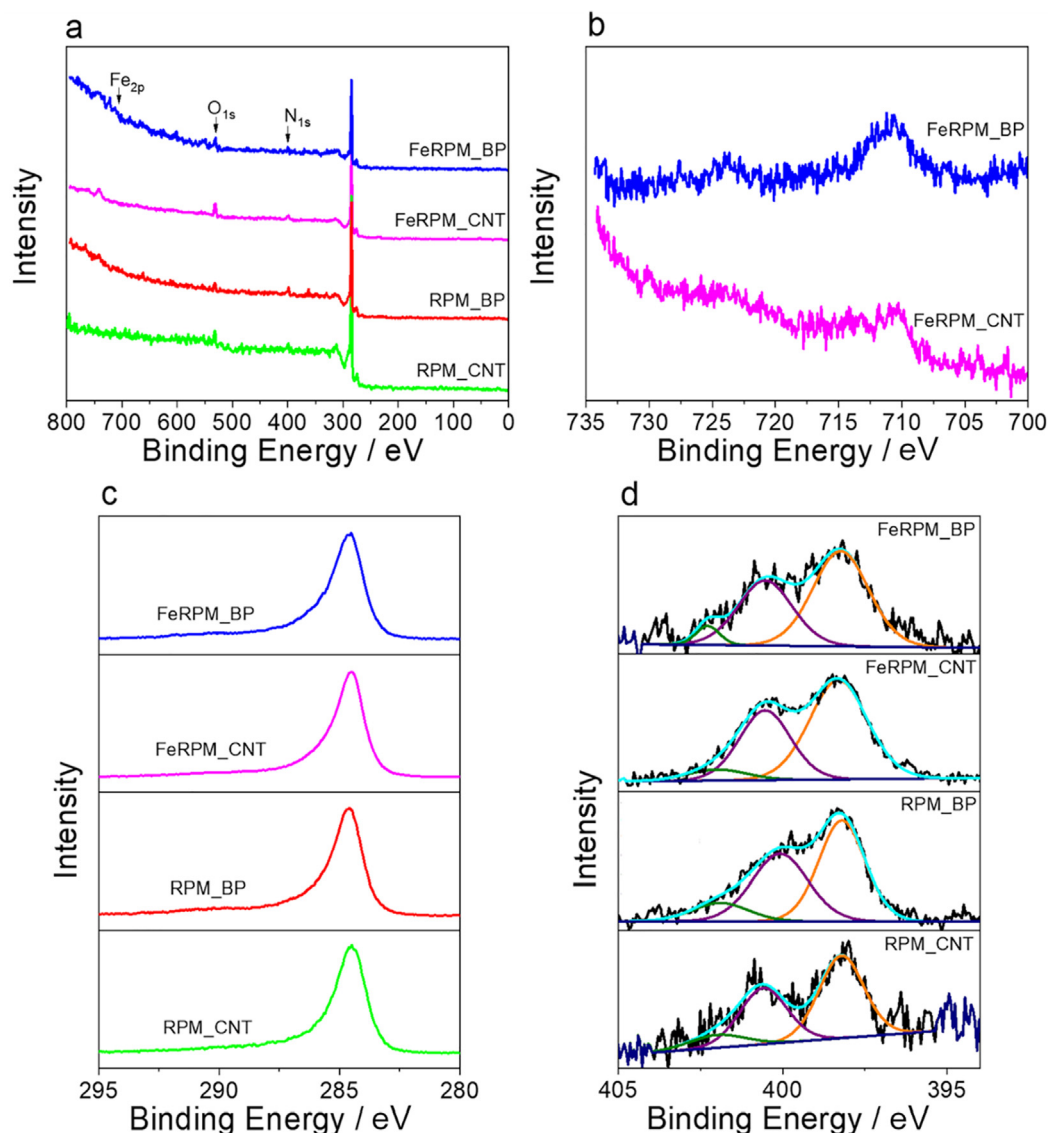

Fig. 3. TEM micrographs of (a, b) FeRPM_BP and (c, d) FeRPM_CNT materials.

Fig. 4. (a) XPS survey spectra of carbon materials. (b) Comparison of the Fe 2p photoemission peaks for FeRPM_BP and FeRPM_CNT materials. (c) C 1s spectra of all four materials. (d) N 1s spectra and best-fit for all prepared materials; (━) N_{py}, (━) Npyr and (━) N_{gr} functionalities.

Table 2

XPS analysis of surface atomic %-content (equivalent to molar-%).

Sample	Atomic %		
	N/C	O/C	Fe/C
RPM_CNT	3.2	5.2	–
RPM_BP	4.7	3.9	–
FeRPM_CNT	4.0	7.7	0.4
FeRPM_BP	4.2	7.3	1.3

for mesoporous materials [70]. In addition, all the isotherms present an appreciable gas uptake from very low p/p0 which is associated with micropore filling. The differences in hysteresis profiles reveal significant differences in pore structure among the materials. The isotherm profile of RPM_BP (Fig. 2**a**) exhibits two capillary condensation steps, suggesting that at least two types of pores contribute to the PSD [31]. The PSD of RPM_BP (Fig. 2**b**) shows two peaks: one sharp and centered at 3.7 nm and a broad one at *ca.* 7 nm. The introduction of Fe into the RPM_BP matrix changes the curvature of the hysteresis profile, approaching the expected shape of a type H1 loop [71] typical of mesoporous car-

bons. The PSD profile is consequently modified showing a reduced amount of pores centered at 3.7 nm and the formation of bigger pores in the range 10–20 nm. The use of MWCNT results in lower specific areas, as previously mentioned, as well as changes in the adsorption isotherms, whose loops approximate the H5 and H4 types for RPM_CNT and FeRPM_CNT respectively (Fig. 2**c**) [71]. The type H5 loop observed for RPM_CNT is associated with pore structures containing both open and partially blocked mesopores [71]; the H4 loop observed for FeRPM_CNT has already been reported for micro-/mesoporous carbons [71]. The PSD in Fig. 2**d** follows a similar trend to that reported for BP based samples after addition of Fe, i.e. that the introduction of Fe results in the disappearance of pores >5 nm.

Fig. 3**a–d** show TEM micrographs of FeRPM_BP (**3a and 3b**) and FeRPM_CNT (**3c and 3d**). CNT agglomerates form an entangled network, whereas BP forms aggregates of spherical nanoparticles as previously reported [56]. Along the walls of CNT it is possible to clearly observe aggregates which we attribute to the formation of Fe particles; this was confirmed via elemental mapping as shown in Supporting Information (**Fig. S1**). Micrographs of FeRPM_CNT at higher magnification (Fig. 3**d**) clearly show that
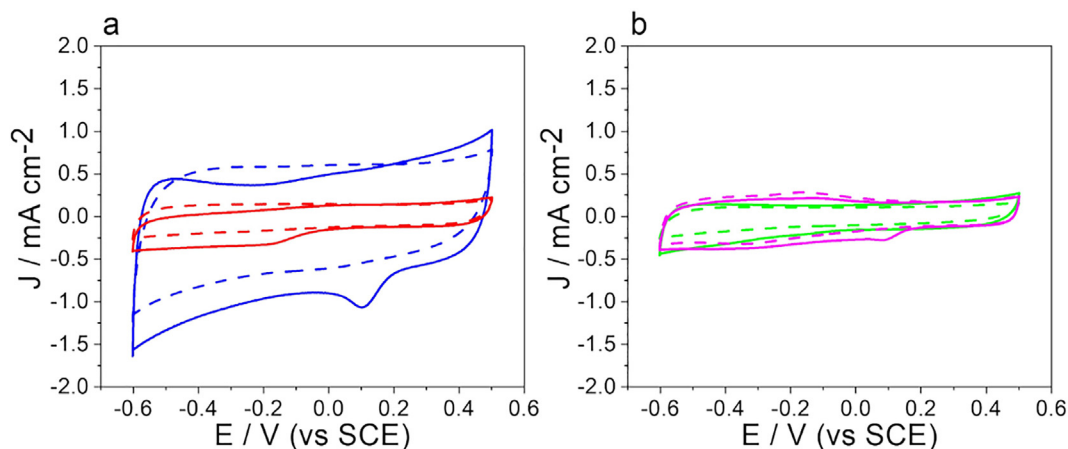
Fig. 5. Cyclic voltammograms obtained in O_2– (solid lines) and N_2-saturated (dashed lines) 0.05 M Na_2HPO_4/ NaH_2PO_4 aqueous solutions (pH 7.2) at 5 mV s^{-1} for electrocatalysts synthesized with (a) BP and (b) CNT as nanocarbon scaffolds; (——) FeRPM_BP, (——) RPM_BP, (——) FeRPM_CNT and (——) RPM_CNT.

CNT are uniformly coated by a resin layer of thickness in the range 9–24 nm. In the case of FeRPM_BP it was not possible to discern the presence of well-defined Fe-rich nanoparticles, while micrographs at high magnification do not show a clear discontinuity between BP scaffold and resin (Fig. 3**b**). This observation suggests that the resin is much thinner and finely distributed over the BP nanoscaffold when compared to CNT. Also, it is consistent with the resin coating resulting in partial pore occlusion and lower BET area than for the bare BP nanocarbon material.

The surface composition was characterized using XPS. Fig. 4**a** shows survey spectra of the four materials; surface atomic ratios calculated from high resolution spectra are summarized in Table 2. Surveys show characteristic peaks associated with C 1s (284 eV), N 1s (400 eV) and O 1s (532 eV). Fe 2p doublets (710 eV) are not discernible in the surveys of FeRPM_BP or FeRPM_CNT; however, their presence was evidenced in the high resolution scans, as shown in Fig. 4**b**. High resolution spectra of the C 1s region (Fig. 4**c**) display a maximum at *ca.* 284 eV characteristic of graphitic carbon and an unresolved asymmetric line that indicates the presence of functional C—N, C—O and C=O groups [38,59,72]. Fig. 4**d** shows high resolution N 1s spectra and their best-fits. Three contributions assigned to pyridinic-N (N_{py}, 398.0–398.3 eV), pyrrolic-N (N_{pyr}, 400.0–400.6 eV) and graphitic-N (N_{gr}, 401.8–402.3 eV) were observed to yield satisfactory fits [59,73,74], thus indicating a mixture of surface N-functionalities with more than 90% of the intensity arising from pyridinic- and pyrrolic-N contributions. High-resolution spectra in the O 1s region are shown in Supporting Information (see **Fig. S2**).

The surface Fe/C atomic ratio values estimated from XPS are <1.5% and similar to those obtained from bulk characterization methods (see Table 1). Given that iron acetate is present in the resorcinol-formadehyde resin component exclusively, this result indicates that in FeRPM_BP and FeRPM_CNT materials are highly nanostructured and that the resin is highly dispersed over the surface of the nanocarbon scaffold, in agreement with previous characterization results.

In summary, the characterization of composite materials indicates that nanocarbon scaffolds in combination with resorcinol–formaldehyde resins results in carbon materials that can incorporate both N-sites and Fe-sites. Use of Black Pearls results in higher specific surface areas and greater exposure of Fe-centers at the surface of the carbonized materials. The performance of these materials as cathodes for the ORR is discussed in the following sections.

3.2. Electrochemical characterization

The materials characterized in the previous section were then studied as potential electrocatalysts for the oxygen reduction reaction (ORR), with a focus on applications as air-cathodes in MFCs. High electrocatalyst activity in electrolytes at near physiological pH is most relevant for MFC applications therefore we tested ORR activity at pH 7.2. Fig. 5**a and b** show cyclic voltammograms for Fe-free and Fe-containing materials, respectively, obtained in 0.05 M Na_2HPO_4/NaH_2PO_4 aqueous solutions at pH 7.2 in the potential range −0.6 to +0.5 V_{SCE} at 5 mV s^{-1}, in the presence (solid lines) and absence (dashed lines) of O_2 in the electrolyte. Fig. 5**a** shows CVs for materials prepared using BP as the nanocarbon scaffold; the CVs show only a capacitive background in Ar-purged solutions, however the presence of O_2 in the electrolyte results in cathodic peaks indicative of the ORR. Importantly, the presence of Fe-centers in FeRPM_BP results in a considerable enhancement of the cathodic peak current ($j_{c,max}$) relative to RPM_BP, as well as in a significant positive shift in the peak potential (E_p) from −0.207 ± 0.021 V_{SCE} to +0.104 ± 0.013 V_{SCE} (ΔE_p > 300 mV), indicative of a lower overpotential for the ORR. Fig. 5**b** shows CVs for materials prepared with MWCNT; as in the previous case, CVs in Ar-purged solutions result in a capacitive response. In the presence of O_2 the CV of RPM_CNT does not yield a resolved redox peak, however with the addition of Fe-centers in FeRPM_CNT it is possible to observe a cathodic peak at E_p = 0.070 ± 0.026 V_{SCE} that indicates activity in the ORR, albeit with a lower cathodic peak current relative to FeRPM_BP. Notably, the E_p value of *ca.* 0.100 V_{SCE} observed for FeRPM_BP and FeRPM_CNT is comparable to that of a commercial Pt/C, observed at +-0.078 ± 0.003 V_{SCE} in the same conditions (see **Supporting Information, Fig. S3**). The relatively modest performance of Pt-based catalysts for ORR in phosphate-rich electrolytes is well reported in the literature [22–24]; results therefore indicate that in these challenging electrolytes, these Fe-based electrocatalysts are promising materials for MFC air-cathodes.

RDE studies were used to further understand activity and selectivity in the ORR. Fig. 6**a** shows a comparison of linear sweeps obtained in O_2-saturated electrolyte at 5 mV s^{-1} and 1600 rpm. Trends in onset potentials and limiting currents obtained via RDE voltammetry are consistent with results from static electrode cyclic voltammetry experiments: Fe-free materials show poor ORR activity, whereas Fe-containing materials show the best onset
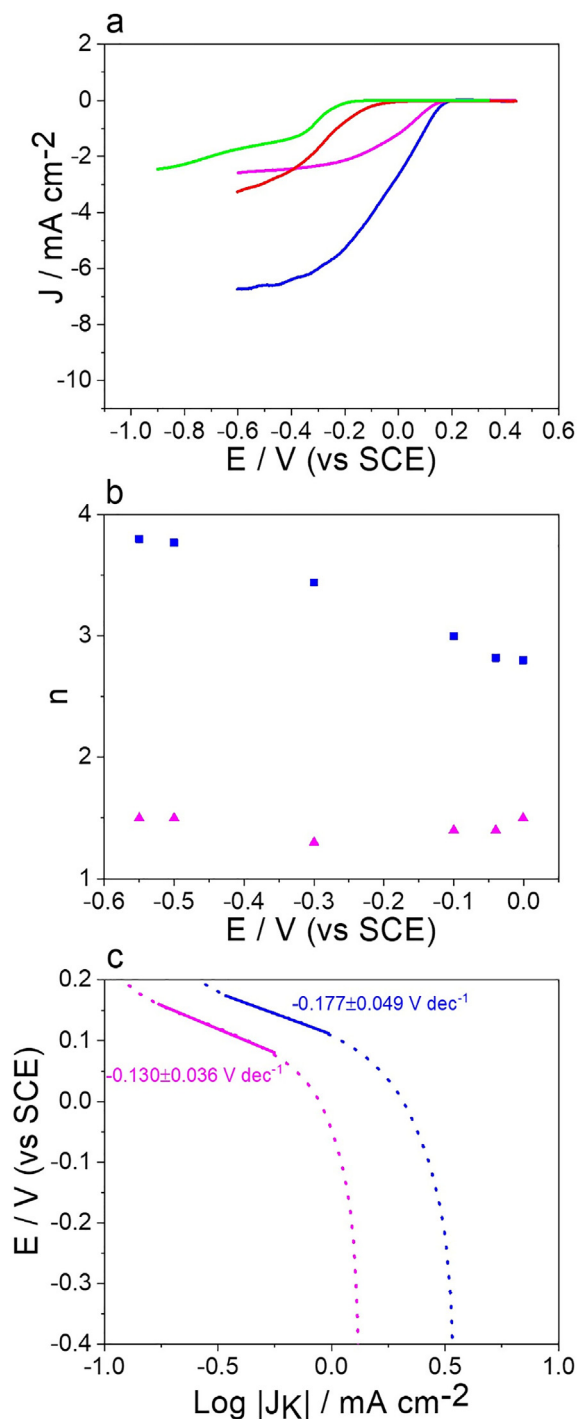
Fig. 6. (a) Comparison of voltammograms for (——) RPM_BP, (——) RPM_CNT, (——) FeRPM_BP and (——) FeRPM_CNT in O_2-saturated 0.05 M Na_2HPO_4/NaH_2PO_4 aqueous solutions (pH 7.2) at 5 mV s^{-1} at 1600 rpm; data are shown after correction for capacitive contributions. (b) number of electrons calculated at different potentials from Koutecky-Levich plots for (■) FeRPM_BP and (▲) FeRPM_CNT. (c) Tafel plot for (——) FeRPM_BP and (——) FeRPM_CNT materials obtained from the voltammograms in (a).

Table 3

Summary of performance indicators obtained for FeRPM_BP and FeRPM_CNT electrode materials in the ORR. E_{onsets} are calculated from RDE voltammetry at 1600 rpm.

	FeRPM_BP	FeRPM_CNT
Cathodic peak potential E_p (V vs SCE)	0.104 ± 0.013	0.070 ± 0.026
E_{onset} @ 0.1 mA cm^{-2} (V vs SCE)	0.153 ± 0.014	0.140 ± 0.006
$E_{1/2}$ @ 1600 rpm (V vs SCE)	−0.076 ± 0.014	−0.08 ± 0.06

approximately half the expected value. Interestingly, the ORR performance of FeRPM_BP is superior to that obtained recently using activated carbon as a scaffold under similar conditions, for which the value of J_{LIM} was significantly smaller compared with our catalysts [75]. Koutecky-Levich analysis of RDE voltammetry as a function of rotation rate, at potentials between 0.0 and −0.6 V vs SCE (see Supporting Information, **Fig. S4**), was used to calculate the average number of electrons, n, involved in the ORR process. Values of n obtained as a function of potential are shown in Fig. 6**b** and indicate that FeRPM_BP displays significantly better selectivity towards the 4e$^-$ ORR pathway.

Tafel plots for Fe-containing materials are shown in Fig. 6**c**; slope values of (0.13 ± 0.04) and (0.18 ± 0.05) V dec^{-1} were obtained for FeRPM_CNT and FeRPM_BP, respectively. These values are somewhat larger than the value of *ca.* 100 mV reported for the ORR at polycrystalline Pt electrodes in near-neutral phosphate aqueous solutions [76], but significantly better than those reported for ORR at Au and pure carbon electrodes at neutral pH [77]. Values of Tafel slope >120 mV can arise from morphology [78] and site-blocking effects [79], and neither can be excluded in the case of the porous FeRPM materials in the presence of phosphate anions.
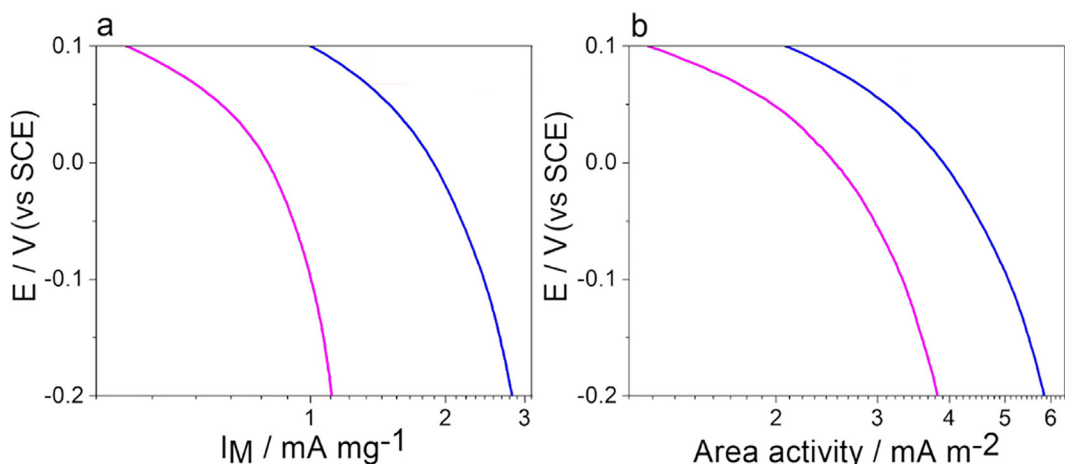
The mass activity and specific area activities of the FeRPM catalysts were also determined and are shown in Fig. 7**a and b**, respectively. In both cases the activity is superior for FeRPM_BP relative to FeRPM_CNT; this suggests that whether the currents are normalized by the mass of catalyst or the specific surface area the FeRPM_BP displays a better intrinsic activity. This is consistent with the greater surface concentration of Fe-centers observed for FeRPM_BP via XPS analysis. Mass activity results are also consistent with final MFC device performances reported in the following section, showing FeRPM_BP as the best cathodic materials and FeRPM_CNT performances aligned with non Fe based materials.

CV, LSV and Koutecky-Levich analysis all indicate that low-cost Black Pearls carbon particles result in superior activity in the ORR when used as nanocarbon scaffolds for the preparation of Fe/N-doped catalysts, compared to MWCNT. XPS data, as well as TEM micrography, suggests that this higher intrinsic activity might be the result of greater dispersion of accessible Fe-sites at the catalyst surface. Notably, the performance indicators determined for FeRPM_BP compare very well also to those obtained in previous work by other groups using other advanced carbon nanomaterials such as N-doped nanotubes, nanofibers and graphene in ORR at near-neutral pH [38,80,81]. It is not possible to unequivocally elucidate the nature of the active sites in these heterogeneous materials, as it is often the case for pyrolyzed Fe-N-C electrocatalysts in the literature. Nonetheless it is important to note that the synthetic approach in this work yields all of the structural motifs hypothesized to play a role in the ORR activity of Fe-N-C materials [82]: carbon encapsulated Fe particles [83,84] and surface pyrrolic- and pyridinic-N functionalities both of which have been proposed to form FeN$_4$ active centers [82,85,86].

3.3. Microbial fuel cells test

All synthesized catalysts were tested in double chamber microbial fuel cell devices. As described in the experimental section, the

potentials. Table 3 reports a summary of onset potential at 0.1 mA cm^{-2} (E_{onset}) and half-wave potential ($E_{1/2}$) values calculated from RDE voltammetry for FeRPM_BP and FeRPM_CNT. Significant differences are observed in J_{LIM} of FeRPM_BP and FeRPM_CNT: FeRPM_BP shows a J_{LIM} close to that expected for a 4-electron ORR reduction pathway whereas FeRPM_CNT displays

Fig. 7. Comparison of mass activity (a) and area activity (b) obtained from RDE voltammetry in O_2-saturated 0.05 M Na_2HPO_4/NaH_2PO_4 aqueous solutions (pH 7.2) at 5 mV s^{-1} at 1600 rpm, for FeRPM_BP and FeRPM_CNT; (——) FeRPM_BP, (——) FeRPM_CNT.
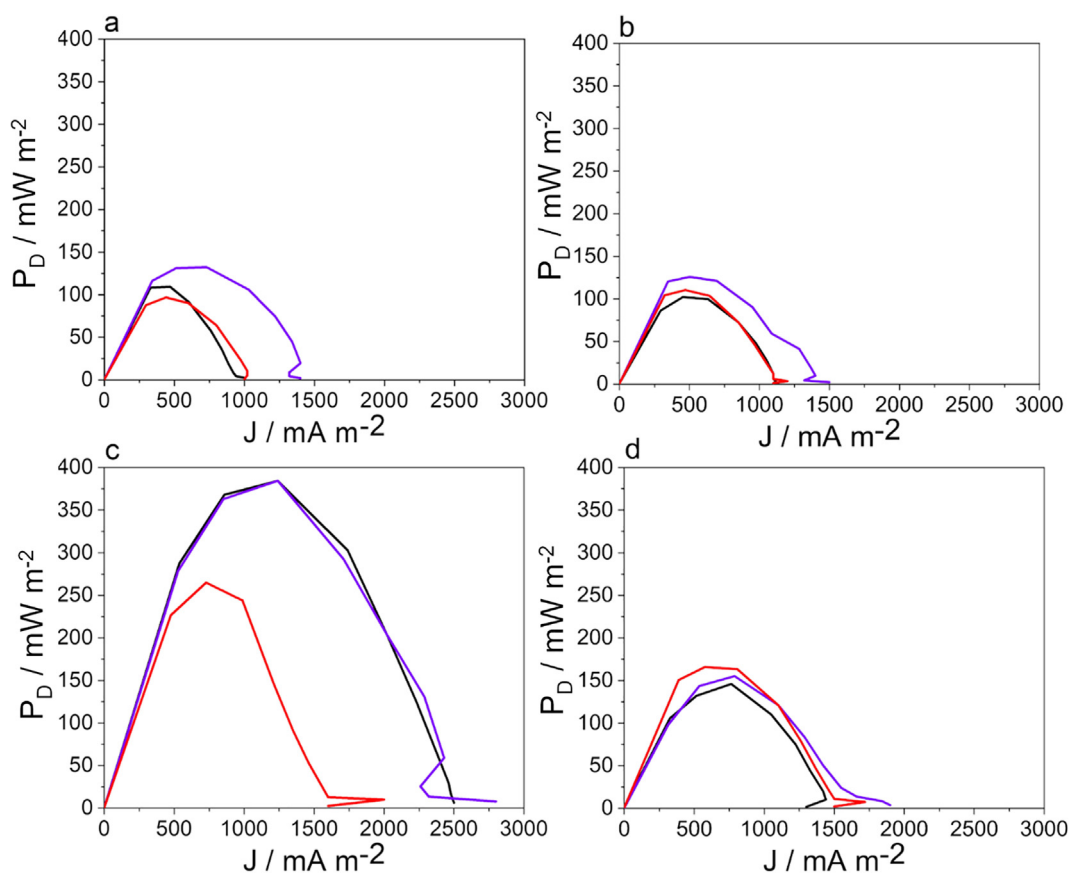
Fig. 8. Power density (P_D) of MFCs equipped with RPM_BP (a), RPM_CNT (b), FeRPM_BP (c) and FeRPM_CNT (d). Curves were obtained with three different acclimated cells to verify the reproducibility of results.

tests were conducted using three different MFCs. Cells were initially acclimated using potassium ferricyanide at the cathode as electron acceptor [4,8] until a stable voltage was obtained. This procedure was employed to minimize the variations caused by possible differences in MFC populations at the anode. Once a stable voltage output was obtained, the cathodic solution was removed and the cathode compartment washed with plenty of Millipore water, before replacing the graphite rod cathode with carbon clothes covered by RPM_BP, RPM_CNT, FeRPM_BP or FeRPM_CNT electrocatalysts prepared as described in the experimental section.

Fig. 8 shows power density curves of three replicate cells assembled with RPM_BP (a), RPM_CNT (b), FeRPM_BP (c) and FeRPM_CNT (d) cathodes. The maximum power density reached by each type of catalyst reflects the results obtained during *ex situ* electrochemical characterization: FeRPM_BP shows peak power densities in the range 250–375 mW m^{-2}, which compare well to typical outputs obtained using acetate as biofuel in the anodic compartment [5,51,87]. Importantly, these outputs were superior to those obtained using commercial Pt/C cathodes in the same MFC devices, under identical conditions as shown in Fig. 9.
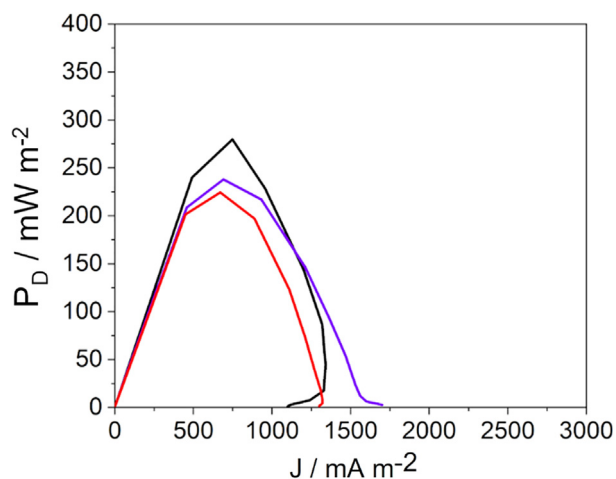
Fig. 9. Power density curves of MFCs equipped with Pt/C. Curves were obtained with three different acclimated cells to confirm the reproducibility of results.

Table 4
Summary of MFC performances reported in literature relative to Pt/C cathodes and compared with this work.

Sample Name	Normalized performance [%]	Ref.
FeRPM_BP	139%	This work
Fe-N-C/AC	200%	[75]
FeE/CNT	54%	
FePc	94%	[51]
FePc	167%	[87]

RPM_BP and RPM_CNT cathodes display similar performances, with peak power density values in the range 96–131 mW m^{-2}. FeRPM_CNT cathodes performed marginally better than Fe-free materials, yielding peak power densities in the range 144–165 mW m^{-2}, i.e. only *ca.* 21% better than the peak power outputs of RPM_BP. To better compare the results obtained, the maximum power densities averages were normalized on Pt/C ones showing 139% for FeRPM_BP, 46% for RPM_BP and RPMCNTs and 63% for FeRPM_CNTs. A direct comparison with other Fe based catalysts is reported in Table 4. Importantly, plain carbon cloth cathodes were also tested, showing negligible MFCs power density outputs (<5 mW m^{-2}, see **Supporting Information, Fig. S5**): this indicates that neither bare carbon cloth nor residual traces of potassium ferricyanide in the cathodic compartment can be at the origin of the activity observed with synthesized cathodes.

Trends in power outputs observed in MFC experiments reflect the results obtained via voltammetry characterization. Cathodic performances were enhanced when Fe-sites were present in the tested materials. Furthermore, FeRPM_BP cathodes performed significantly better than FeRPM_CNT ones and, notably, better than Pt/C cathodes under identical conditions. The results indicate that the combination of high number of available surface sites and increased dispersion of Fe-sites through the introduction of the BP scaffold translates into enhanced power outputs once the materials are integrated into MFC devices. Optimisation of the device design, e.g. by adoption of a single-chamber configuration [75] should further improve power outputs to fully take advantage of electrocatalyst performance. This indicates that employment of the proposed synthesis with a low cost amorphous carbon template offers an effective route for the preparation of highly active cathodic materials for MFCs.

4. Conclusions

We have designed highly mesoporous carbon based catalysts with high catalytic efficiency towards the oxygen reduction reaction in neutral media through a hydrothermal process. The samples underwent thermal annealing under NH$_3$ rich atmosphere to incorporate N defects in the materials synthesized with two different proposed scaffolds. XPS and elemental analysis results showed that iron and nitrogen contents vary on the basis of the carbon scaffold used during the synthesis. XPS analysis also suggests that nitrogen incorporation into the proposed scaffolds produces high density of pyridinic and graphitic sites. XRD analysis revealed that multiwalled carbon nanotubes allowed the production of a highly crystalline structure whereas a more amorphous phase is observed for the carbon signal when Black Pearls is employed. N$_2$ sorption isotherms revealed mesoporosity and high surface area values for Black Pearls based samples. Iron introduction was found to promote graphitization and pore opening, leading to a surface area decrease and sharper XRD peaks, furthermore iron introduction drastically changed the catalytic activity towards the ORR as reported by the electrochemical characterization. Nevertheless, iron incorporation using the two different scaffold precursors proposed led to a different catalytic response, with Black Pearls based templates providing better dispersion of catalytic centers and a higher amount of available active sites, thus indicating the importance of the carbon morphology on the ORR catalysis. Microbial Fuel Cell tests report maximum power density performances more than 3 times higher than non Fe based samples, if Fe is combined with Black Pearls, thus confirming preliminary electrochemical *ex situ* results. The synthesis optimization allowed the production of an efficient catalyst based on low-cost black pearls (1/100 than the cost of multiwalled carbon nanotubes) as the carbon template. The optimized material also demonstrated performance comparable with that of commercial platinum on carbon electrodes used as reference. In summary, we demonstrated, through an efficient and low-cost synthesis, the development of an ORR Fe-based catalyst efficient in neutral conditions, of interest for application in microbial bioelectrochemical systems. Optimizations and scale up procedures of the designed cathode will further decrease the price/Watt ratio and allow the large scale production of non-precious and sustainable catalytic electrodes for abiotic Oxygen Reduction Reaction in Microbial Fuel Cells.

Declaration of Competing Interest

The authors declare that they have no known competing financial interests or personal relationships that could have appeared to influence the work reported in this paper.

Acknowledgements

References

[1] E.C. Horizon, Work Programme 2018–2020.

[2] A. Iannaci, T.P. Sciarria, B. Mecheri, F. Adani, S. Licoccia, A. D'Epifanio, Power generation using a low-cost sulfated zirconium oxide based cathode in single chamber microbial fuel cells, J. Alloys Compd. 693 (2017) 170–176.

[3] N.L. Panwar, S.C. Kaushik, S. Kothari, Role of renewable energy sources in environmental protection: a review, Renew. Sust. Energ. Rev. 15 (2011) 1513–1524.

[4] B.E. Logan, B. Hamelers, R. Rozendal, U. Schröder, J. Keller, S. Freguia, P. Aelterman, W. Verstraete, K. Rabaey, Microbial fuel cells: methodology and technology, Environ. Sci. Technol. 40 (2006) 5181–5192.

[5] M.-T. Nguyen, B. Mecheri, A. D'Epifanio, T.P. Sciarria, F. Adani, S. Licoccia, Iron chelates as low-cost and effective electrocatalyst for oxygen reduction reaction in microbial fuel cells, Int. J. Hydrogen Energy 39 (2014) 6462–6469.

[6] K.-D. Kreuer, Fuel Cells: Selected Entries from the Encyclopedia of Sustainability Science and Technology, Springer Science & Business Media, 2012.

[7] A. Kumar, L.-H.-H. Hsu, P. Kavanagh, F. Barrière, P.N. Lens, L. Lapinsonnière, U. Schröder, X. Jiang, D. Leech, The ins and outs of microorganism–electrode electron transfer reactions, Nat. Rev. Chem. 1 (2017) 0024.

[8] A. Iannaci, A. Myles, T. Flinois, J.A. Behan, F. Barrière, E.M. Scanlan, P.E. Colavita, Tailored glycosylated anode surfaces: addressing the exoelectrogen bacterial community via functional layers for microbial fuel cell applications, Bioelectrochemistry 136 (2020) 107621.

[9] C. Santoro, C. Arbizzani, B. Erable, I. Ieropoulos, Microbial fuel cells: From fundamentals to applications. A review, J. Power Sources 356 (2017) 225–244.

[10] L. Lapinsonnière, M. Picot, C. Poriel, F. Barrière, Phenylboronic acid modified anodes promote faster biofilm adhesion and increase microbial fuel cell performances, Electroanalysis 25 (2013) 601–605.

[11] M. Picot, L. Lapinsonnière, M. Rothballer, F. Barrière, Graphite anode surface modification with controlled reduction of specific aryl diazonium salts for improved microbial fuel cells power output, Biosens. Bioelectron. 28 (2011) 181–188.

[12] H. Smida, E. Lebègue, J.-F. Bergamini, F. Barrière, C. Lagrost, Reductive electrografting of in situ produced diazopyridinium cations: tailoring the interface between carbon electrodes and electroactive bacterial films, Bioelectrochemistry 120 (2018) 157–165.

[13] H. Smida, E. Lebègue, M. Cortes, J.-F. Bergamini, F. Barrière, C. Lagrost, Corrigendum to "Reductive electrografting of in situ produced diazopyridinium cations: Tailoring the interface between carbon electrodes and electroactive bacterial films" [Bioelectrochem. 120 (2018) 157–165], Bioelectrochemistry 125 (2019) 70.

[14] A. Kuzume, U. Zhumaev, J. Li, Y. Fu, M. Füeg, A. Esteve-Nuñez, T. Wandlowski, An in-situ surface electrochemistry approach toward whole-cell studies: Charge transfer between Geobacter sulfurreducens and electrified metal/electrolyte interfaces through linker molecules, Electrochim. Acta 112 (2013) 933–942.

[15] K. Guo, S. Freguia, P.G. Dennis, X. Chen, B.C. Donose, J. Keller, J.J. Gooding, K. Rabaey, Effects of surface charge and hydrophobicity on anodic biofilm formation, community composition, and current generation in bioelectrochemical systems, Environ. Sci. Technol. 47 (2013) 7563–7570.

[16] K. Guo, A. Prévoteau, S.A. Patil, K. Rabaey, Engineering electrodes for microbial electrocatalysis, Curr. Opinion Biotechnol. 33 (2015) 149–156.

[17] M.K. Debe, Electrocatalyst approaches and challenges for automotive fuel cells, Nature 486 (2012) 43.

[18] H.-H. Yang, R.L. McCreery, Elucidation of the mechanism of dioxygen reduction on metal-free carbon electrodes, J. Electrochem. Soc. 147 (2000) 3420.

[19] E. Yeager, Electrocatalysts for O2 reduction, Electrochim. Acta 29 (1984) 1527–1537.

[20] B. Šljukić, C.E. Banks, R.G. Compton, An overview of the electrochemical reduction of oxygen at carbon-based modified electrodes, J. Iran. Chem. Soc. 2 (2005) 1–25.

[21] R.A. Rozendal, H.V.M. Hamelers, K. Rabaey, J. Keller, C.J.N. Buisman, Towards practical implementation of bioelectrochemical wastewater treatment, Trends Biotechnol. 26 (2008) 450–459.

[22] Q. He, B. Shyam, M. Nishijima, D. Ramaker, S. Mukerjee, Mitigating phosphate anion poisoning of cathodic Pt/C catalysts in phosphoric acid fuel cells, J. Phys. Chem. C 117 (2013) 4877–4887.

[23] Q. He, X. Yang, W. Chen, S. Mukerjee, B. Koel, S. Chen, Influence of phosphate anion adsorption on the kinetics of oxygen electroreduction on low index Pt (hkl) single crystals, Phys. Chem. Chem. Phys. 12 (2010) 12544–12555.

[24] R. Gisbert, G. García, M.T.M. Koper, Adsorption of phosphate species on poly-oriented Pt and Pt(111) electrodes over a wide range of pH, Electrochim. Acta 55 (2010) 7961–7968.

[25] F. Harnisch, S. Wirth, U. Schröder, Effects of substrate and metabolite crossover on the cathodic oxygen reduction reaction in microbial fuel cells: platinum vs. iron(II) phthalocyanine based electrodes, Electrochem. Commun. 11 (2009) 2253–2256.

[26] F. Zhao, F. Harnisch, U. Schröder, F. Scholz, P. Bogdanoff, I. Herrmann, Challenges and constraints of using oxygen cathodes in microbial fuel cells, Environ. Sci. Technol. 40 (2006) 5193–5199.

[27] K.N. Wood, R. O'Hayre, S. Pylypenko, Recent progress on nitrogen/carbon structures designed for use in energy and sustainability applications, Energy Environ. Sci. 7 (2014) 1212–1249.

[28] C. Domìnguez, J.A. Behan, P.E. Colavita, Electrocatalysis at nanocarbons: Model systems and applications in energy conversion, in: N. Yang, G. Zhao, J.S. Foord (Eds.), Nanocarbon Electrochemistry, John Wiley & Sons Ltd, Chichester, 2020, pp. 201–249.

[29] J. Zhang, PEM Fuel Cell Electrocatalysts and Catalyst Layers: Fundamentals and Applications, Springer Science & Business Media, 2008.

[30] L. Timperman, Y.J. Feng, W. Vogel, N. Alonso-Vante, Substrate effect on oxygen reduction electrocatalysis, Electrochim. Acta 55 (2010) 7558–7563.

[31] G. Ferrero, K. Preuss, A. Fuertes, M. Sevilla, M.-M. Titirici, The influence of pore size distribution on the oxygen reduction reaction performance in nitrogen doped carbon microspheres, J. Mater. Chem. A 4 (2016) 2581–2589.

[32] L. Zhao, N. Baccile, S. Gross, Y. Zhang, W. Wei, Y. Sun, M. Antonietti, M.-M. Titirici, Sustainable nitrogen-doped carbonaceous materials from biomass derivatives, Carbon 48 (2010) 3778–3787.

[33] L. Zhao, L.-Z. Fan, M.-Q. Zhou, H. Guan, S. Qiao, M. Antonietti, M.-M. Titirici, Nitrogen-containing hydrothermal carbons with superior performance in supercapacitors, Adv. Mater. (Weinheim, Ger.) 22 (2010) 5202–5206.

[34] L. Zhao, R. He, K.T. Rim, T. Schiros, K.S. Kim, H. Zhou, C. Gutiérrez, S.P. Chockalingam, C.J. Arguello, L. Pálová, D. Nordlund, M.S. Hybertsen, D.R. Reichman, T.F. Heinz, P. Kim, A. Pinczuk, G.W. Flynn, A.N. Pasupathy, Visualizing individual nitrogen dopants in monolayer graphene, Science 333 (2011) 999.

[35] K.-H. Wu, D.-W. Wang, X. Zong, B. Zhang, Y. Liu, I.R. Gentle, D.-S. Su, Functions in cooperation for enhanced oxygen reduction reaction: the independent roles of oxygen and nitrogen sites in metal-free nanocarbon and their functional synergy, J. Mater. Chem. A 5 (2017) 3239–3248.

[36] J.A. Behan, A. Iannaci, C. Domínguez, S.N. Stamatin, M.K. Hoque, J.M. Vasconcelos, T.S. Perova, P.E. Colavita, Electrocatalysis of N-doped carbons in the oxygen reduction reaction as a function of pH: N-sites and scaffold effects, Carbon 148 (2019) 224–230.

[37] J.A. Behan, E. Mates-Torres, S.N. Stamatin, C. Domínguez, A. Iannaci, K. Fleischer, M.K. Hoque, T.S. Perova, M. García-Melchor, P.E. Colavita, Untangling cooperative effects of pyridinic and graphitic nitrogen sites at metal-free N-doped carbon electrocatalysts for the oxygen reduction reaction, Small 15 (2019) 1902081.

[38] B. Mecheri, V.C. Ficca, M.A.C. de Oliveira, A. D'Epifanio, E. Placidi, F. Arciprete, S. Licoccia, Facile synthesis of graphene-phthalocyanine composites as oxygen reduction electrocatalysts in microbial fuel cells, Appl. Catal., B 237 (2018) 699–707.

[39] L. Feng, Y. Yan, Y. Chen, L. Wang, Nitrogen-doped carbon nanotubes as efficient and durable metal-free cathodic catalysts for oxygen reduction in microbial fuel cells, Energy Environ. Sci. 4 (2011) 1892–1899.

[40] X. Yang, W. Zou, Y. Su, Y. Zhu, H. Jiang, J. Shen, C. Li, Activated nitrogen-doped carbon nanofibers with hierarchical pore as efficient oxygen reduction reaction catalyst for microbial fuel cells, J. Power Sources 266 (2014) 36–42.

[41] L. Feng, Y. Chen, L. Chen, Easy-to-operate and low-temperature synthesis of gram-scale nitrogen-doped graphene and its application as cathode catalyst in microbial fuel cells, ACS Nano 5 (2011) 9611–9618.

[42] M.-T. Nguyen, B. Mecheri, A. Iannaci, A. D'Epifanio, S. Licoccia, Iron/polyindole-based electrocatalysts to enhance oxygen reduction in microbial fuel cells, Electrochim. Acta 190 (2016) 388–395.

[43] A. Iannaci, B. Mecheri, A. D'Epifanio, M.J.L. Elorri, S. Licoccia, Iron–nitrogen-functionalized carbon as efficient oxygen reduction reaction electrocatalyst in microbial fuel cells, Int. J. Hydrogen Energy 41 (2016) 19637–19644.

[44] S. Cheng, H. Liu, B.E. Logan, Power densities using different cathode catalysts (Pt and CoTMPP) and polymer binders (Nafion and PTFE) in single chamber microbial fuel cells, Environ. Sci. Technol. 40 (2006) 364–369.

[45] J.-N. Zhang, S.-J. You, Y.-X. Yuan, Q.-L. Zhao, G.-D. Zhang, Efficient electrocatalysis of cathodic oxygen reduction with Pt–Fe alloy catalyst in microbial fuel cell, Electrochem. Commun. 13 (2011) 903–905.

[46] B. Mecheri, A. Iannaci, A. D'Epifanio, M.J. Nieto-Monge, M.J. Lazaro, S. Licoccia, Iron-based electrocatalysts supported on nanostructured carbon to enhance oxygen reduction in microbial fuel cells, ECS Trans. 72 (2016) 9–15.

[47] X. Li, B. Hu, S. Suib, Y. Lei, B. Li, Manganese dioxide as a new cathode catalyst in microbial fuel cells, J. Power Sources 195 (2010) 2586–2591.

[48] N. Duteanu, B. Erable, S.M. Senthil Kumar, M.M. Ghangrekar, K. Scott, Effect of chemically modified Vulcan XC-72R on the performance of air-breathing cathode in a single-chamber microbial fuel cell, Bioresour. Technol. 101 (2010) 5250–5255.

[49] L. Wang, P. Liang, J. Zhang, X. Huang, Activity and stability of pyrolyzed iron ethylenediaminetetraacetic acid as cathode catalyst in microbial fuel cells, Bioresour. Technol. 102 (2011) 5093–5097.

[50] P. Aelterman, M. Versichele, E. Genettello, K. Verbeken, W. Verstraete, Microbial fuel cells operated with iron-chelated air cathodes, Electrochim. Acta 54 (2009) 5754–5760.

[51] L. Birry, P. Mehta, F. Jaouen, J.-P. Dodelet, S. Guiot, B. Tartakovsky, Application of iron-based cathode catalysts in a microbial fuel cell, Electrochim. Acta 56 (2011) 1505–1511.

[52] G. Massaglia, V. Margaria, A. Sacco, M. Castellino, A. Chiodoni, F.C. Pirri, M. Quaglio, N-doped carbon nanofibers as catalyst layer at cathode in single chamber Microbial Fuel Cells, Int. J. Hydrogen Energy 44 (2019) 4442–4449.

[53] G. Massaglia, A. Sacco, M. Castellino, A. Chiodoni, F. Frascella, S. Bianco, C.F. Pirri, M. Quaglio, N-doping modification by plasma treatment in polyacrylonitrile derived carbon-based nanofibers for Oxygen Reduction Reaction, Int. J. Hydrogen Energy 46 (2021) 13845–13854.

[54] C. Santoro, A. Stadlhofer, V. Hacker, G. Squadrito, U. Schröder, B. Li, Activated carbon nanofibers (ACNF) as cathode for single chamber microbial fuel cells (SCMFCs), J. Power Sources 243 (2013) 499–507.

[55] C.M. Long, M.A. Nascarella, P.A. Valberg, Carbon black vs. black carbon and other airborne materials containing elemental carbon: physical and chemical distinctions, Environ. Pollut. 181 (2013) 271–286.

[56] A. Macías-García, M.A. Díaz-Díez, M. Alfaro-Domínguez, J.P. Carrasco-Amador, Influence of chemical composition, porosity and fractal dimension on the electrical conductivity of carbon blacks, Heliyon 6 (2020) e04024.

[57] W.-C. Chang, M.T. Nguyen, Investigations of a platinum–ruthenium/carbon nanotube catalyst formed by a two-step spontaneous deposition method, J. Power Sources 196 (2011) 5811–5816.

[58] T. Schilling, M. Bron, Oxygen reduction at Fe–N-modified multi-walled carbon nanotubes in acidic electrolyte, Electrochim. Acta 53 (2008) 5379–5385.

[59] J.A. Behan, M.K. Hoque, S.N. Stamatin, T.S. Perova, L. Vilella-Arribas, M. García-Melchor, P.E. Colavita, Experimental and computational study of dopamine as an electrochemical probe of the surface nanostructure of graphitized N-doped carbon, J. Phys. Chem. C 122 (2018) 20763–20773.

[60] C. Domínguez, K.M. Metz, M.K. Hoque, M.P. Browne, L. Esteban-Tejeda, C.K. Livingston, S. Lian, T.S. Perova, P.E. Colavita, Continuous flow synthesis of platinum nanoparticles in porous carbon as durable and methanol-tolerant electrocatalysts for the oxygen reduction reaction, ChemElectroChem 5 (2018) 62–70.

[61] B. Mecheri, A. Iannaci, A. D'Epifanio, A. Mauri, S. Licoccia, Carbon-supported zirconium oxide as a cathode for microbial fuel cell applications, ChemPlusChem 81 (2016) 80–85.

[62] M. Karthik, A. Faik, S. Doppiu, V. Roddatis, B. D'Aguanno, A simple approach for fabrication of interconnected graphitized macroporous carbon foam with uniform mesopore walls by using hydrothermal method, Carbon 87 (2015) 434–443.

[63] S. Marzorati, J.M. Vasconcelos, J. Ding, M. Longhi, P.E. Colavita, Template-free ultraspray pyrolysis synthesis of N/Fe-doped carbon microspheres for oxygen reduction electrocatalysis, J. Mater. Chem. A 3 (2015) 18920–18927.

[64] T.-F. Hung, M.-H. Tu, C.-W. Tsai, C.-J. Chen, R.-S. Liu, W.-R. Liu, M.-Y. Lo, Influence of pyrolysis temperature on oxygen reduction reaction activity of carbon-incorporating iron nitride/nitrogen-doped graphene nanosheets catalyst, Int. J. Hydrogen Energy 38 (2013) 3956–3962.

[65] C.-C. Liu, A.B. Walters, M.A. Vannice, Measurement of electrical properties of a carbon black, Carbon 33 (1995) 1699–1708.

[66] M. Carmo, A.R. dos Santos, J.G.R. Poco, M. Linardi, Physical and electrochemical evaluation of commercial carbon black as electrocatalysts supports for DMFC applications, J. Power Sources 173 (2007) 860–866.

[67] M.E. Birch, T.A. Ruda-Eberenz, M. Chai, R. Andrews, R.L. Hatfield, Properties that influence the specific surface areas of carbon nanotubes and nanofibers, Ann. Occup. Hyg. 57 (2013) 1148–1166.

[68] K. Lotz, A. Wütscher, H. Düdder, C.M. Berger, C. Russo, K. Mukherjee, G. Schwaab, M. Havenith, M. Muhler, Tuning the properties of iron-doped porous graphitic carbon synthesized by hydrothermal carbonization of cellulose and subsequent pyrolysis, ACS Omega 4 (2019) 4448–4460.

[69] W. Xia, V. Hagen, S. Kundu, Y. Wang, C. Somsen, G. Eggeler, G. Sun, G. Grundmeier, M. Stratmann, M. Muhler, Controlled etching of carbon nanotubes by iron-catalyzed steam gasification, Adv. Mater. (Weinheim, Ger.) 19 (2007) 3648–3652.

[70] K.S. Sing, Reporting physisorption data for gas/solid systems with special reference to the determination of surface area and porosity (Recommendations 1984), Pure Appl. Chem. 57 (1985) 603–619.

[71] M. Thommes, K. Kaneko, A.V. Neimark, J.P. Olivier, F. Rodriguez-Reinoso, J. Rouquerol, K.S. Sing, Physisorption of gases, with special reference to the evaluation of surface area and pore size distribution (IUPAC Technical Report), Pure Appl. Chem. 87 (2015) 1051–1069.

[72] C. Alegre, M.E. Gálvez, E. Baquedano, R. Moliner, E. Pastor, M.J.s. Lázaro, Oxygen-functionalized highly mesoporous carbon xerogel based catalysts for direct methanol fuel cell anodes, J. Phys. Chem. C 117 (2013) 13045–13058.

[73] P. Serp, J.L. Figueiredo, Carbon Materials for Catalysis, John Wiley & Sons, Hoboken, New Jersey, 2009.

[74] J.A. Behan, S.N. Stamatin, M.K. Hoque, G. Ciapetti, F. Zen, L. Esteban-Tejeda, P.E. Colavita, Combined optoelectronic and electrochemical study of nitrogenated carbon electrodes, J. Phys. Chem. C 121 (2017) 6596–6604.

[75] W. Yang, B.E. Logan, Immobilization of a metal–nitrogen–carbon catalyst on activated carbon with enhanced cathode performance in microbial fuel cells, ChemSusChem 9 (2016) 2226–2232.

[76] T. Shinagawa, K. Takanabe, Impact of solute concentration on the electrocatalytic conversion of dissolved gases in buffered solutions, J. Power Sources 287 (2015) 465–471.

[77] G. Gotti, K. Fajerwerg, D. Evrard, P. Gros, Kinetics of dioxygen reduction on gold and glassy carbon electrodes in neutral media, Int. J. Electrochem. Sci. 8 (2013) 12643–12657.

[78] M.P. Browne, J.M. Vasconcelos, J. Coelho, M. O'Brien, A.A. Rovetta, E.K. McCarthy, H. Nolan, G.S. Duesberg, V. Nicolosi, P.E. Colavita, M.E.G. Lyons, Improving the performance of porous nickel foam for water oxidation using hydrothermally prepared Ni and Fe metal oxides, Sustain. Energy Fuels 1 (2017) 207–216.

[79] A. Holewinski, S. Linic, Elementary mechanisms in electrocatalysis: revisiting the ORR Tafel slope, J. Electrochem. Soc. 159 (2012) H864.

[80] S. Maldonado, K.J. Stevenson, Influence of nitrogen doping on oxygen reduction electrocatalysis at carbon nanofiber electrodes, J. Phys. Chem. B 109 (2005) 4707–4716.

[81] J.D. Wiggins-Camacho, K.J. Stevenson, Mechanistic discussion of the oxygen reduction reaction at nitrogen-doped carbon nanotubes, J. Phys. Chem. C 115 (2011) 20002–20010.

[82] T. Marshall-Roth, N.J. Libretto, A.T. Wrobel, K.J. Anderton, M.L. Pegis, N.D. Ricke, T.V. Voorhis, J.T. Miller, Y. Surendranath, A pyridinic Fe-N4 macrocycle models the active sites in Fe/N-doped carbon electrocatalysts, Nat. Commun. 11 (2020) 5283.

[83] J.A. Varnell, E.C.M. Tse, C.E. Schulz, T.T. Fister, R.T. Haasch, J. Timoshenko, A.I. Frenkel, A.A. Gewirth, Identification of carbon-encapsulated iron nanoparticles as active species in non-precious metal oxygen reduction catalysts, Nat. Commun. 7 (2016) 12582.

[84] K. Strickland, E. Miner, Q. Jia, U. Tylus, N. Ramaswamy, W. Liang, M.-T. Sougrati, F. Jaouen, S. Mukerjee, Highly active oxygen reduction non-platinum group metal electrocatalyst without direct metal–nitrogen coordination, Nat. Commun. 6 (2015) 7343.

[85] A. Zitolo, V. Goellner, V. Armel, M.-T. Sougrati, T. Mineva, L. Stievano, E. Fonda, F. Jaouen, Identification of catalytic sites for oxygen reduction in iron- and nitrogen-doped graphene materials, Nat. Mater. 14 (2015) 937–942.

[86] Q. Jia, N. Ramaswamy, U. Tylus, K. Strickland, J. Li, A. Serov, K. Artyushkova, P. Atanassov, J. Anibal, C. Gumeci, S.C. Barton, M.-T. Sougrati, F. Jaouen, B. Halevi, S. Mukerjee, Spectroscopic insights into the nature of active sites in iron–nitrogen–carbon electrocatalysts for oxygen reduction in acid, Nano Energy 29 (2016) 65–82.

[87] E. HaoYu, S. Cheng, K. Scott, B. Logan, Microbial fuel cell performance with non-Pt cathode catalysts, J. Power Sources 171 (2007) 275–281.